Article

Reconstructed Orthorhombic V_2O_5 Polyhedra for Fast Ion Diffusion in K-Ion Batteries

Yun-Hai Zhu, Qi Zhang, Xu Yang, ..., Xi-Qian Yu, Jun-Min Yan, Qing Jiang

junminyan@jlu.edu.cn

HIGHLIGHTS

Bilayered δ-$K_{0.51}V_2O_5$ nanobelts were developed via reconstruction of α-V_2O_5

A new phase was reversibly generated upon K insertion and extraction

Large interlayer space and optimized growth orientation enabled fast K^+ diffusion

To unlock the compact structure of α-V_2O_5 for the diffusion of K^+, we developed single-crystalline bilayered δ-$K_{0.51}V_2O_5$ nanobelts via reconstruction of α-V_2O_5. Benefiting from the large interlayer space and optimized growth orientation, δ-$K_{0.51}V_2O_5$ exhibits suitable accommodation sites and fast diffusion paths for K^+, enabling high capacity and rate capability. Additionally, the achievement of a high-energy- and high-power-density full K-ion battery proves its feasibility in large-scale energy storage systems.

Article

Reconstructed Orthorhombic V$_2$O$_5$ Polyhedra for Fast Ion Diffusion in K-Ion Batteries

Yun-Hai Zhu,[1,4] Qi Zhang,[2,4] Xu Yang,[1,2] En-Yue Zhao,[3] Tao Sun,[2] Xin-Bo Zhang,[2] Sai Wang,[1] Xi-Qian Yu,[3] Jun-Min Yan,[1,5,*] and Qing Jiang[1]

SUMMARY

Potassium-ion batteries (KIBs) are a promising alternative to lithium-ion batteries because of the abundance, low cost, and redox potential of K; however, the significantly larger radius of K$^+$ inevitably destabilizes the crystal structure of the cathode material, impeding the diffusion of K$^+$. Here, to lower the insertion energetics and diffusion barriers of K$^+$, we synthesized δ-K$_{0.51}$V$_2$O$_5$ nanobelts (KVOs) with a large interlayered structure and optimized growth orientation by reconstructing the V–O polyhedra of orthorhombic V$_2$O$_5$; these exhibited a high average voltage (3.2 V), high capacity (131 mAh g^{-1}), and superior rate capability even at 10 A g^{-1}. By coupling the electrochemical experiments with theoretical calculations, we found that the excellent K-ion storage performance of KVO is attributed to its large interlayered structure and unique 1D morphology. Additionally, we assembled a full KIB composed of KVO and graphite with high energy and power densities, proving its feasibility as a promising new battery.

INTRODUCTION

With the rapid development of renewable energy sources such as solar and wind, a large-scale energy storage system for integration with these sources is highly desired.[1] As the most popular energy storage technology, rechargeable Li-ion batteries (LIBs) are expected to contribute to the solution; however, the use of Li is impeded by its high cost, limited reserves, and uneven distribution.[2] Recently, research has turned to batteries composed of low-cost and earth-abundant elements, including Na, K, Mg, and Al, which are extremely favorable for energy storage systems.[3–6] Among them, emerging potassium-ion batteries (KIBs) have attracted increasing interest as an appealing alternative to LIBs because of the low standard potential of K/K$^+$ (−2.92 V versus standard hydrogen electrode) and high natural abundance of K.[7–10] Unlike sodium-ion batteries (SIBs), which are limited by the lack of suitable anode materials, conventional carbon materials, such as graphite and soft and hard carbon, can be used as anode materials for KIBs. However, the significantly larger radius of the K ion (Li$^+$ < Na$^+$ < K$^+$, 0.76 < 1.02 < 1.38 Å) causes greater structural changes and distortions in the host structure upon insertion and removal, which often results in short cycle life and, in particular, poor rate capability of the cathode material.[11,12] Up until now, very few promising KIB cathode materials have been successfully demonstrated, although positive examples include KVPO$_4$F, K$_3$V$_2$(PO$_4$)$_3$, Prussian blue analogs, K$_{0.7}$Fe$_{0.5}$Mn$_{0.5}$O$_2$, K$_{0.6}$CoO$_2$, K$_{0.5}$MnO$_2$, and K$_{0.5}$V$_2$O$_5$.[13–20] However, achieving high capacity and average voltage, especially in conjunction with high power density, remains a daunting challenge.

The Bigger Picture

As a result of increased energy demand and the prices of fossil fuels, rational use of renewable energy sources has become a growing global concern. Rechargeable potassium-ion batteries (KIBs) are emerging as a promising large-scale energy storage system for storing renewable energy because of the abundance and low cost of potassium resources. However, the significantly larger radius of K$^+$ destabilizes the crystal structure of host materials, impeding the successful application of KIBs. Here, to unlock the compact structure of α-V$_2$O$_5$ for the diffusion of K$^+$, we developed single-crystalline bilayered δ-K$_{0.51}$V$_2$O$_5$ nanobelts (KVOs) via reconstruction of α-V$_2$O$_5$ and achieved excellent K-storage performance. Importantly, the high-energy- and high-power-density KIB constructed with KVO and graphite proves its feasibility in large-scale energy storage systems.

Orthorhombic vanadium pentoxide (α-V_2O_5) is a representative intercalation host and has been used in LIBs and SIBs because of its low cost and ability to exist in different oxidation states from V^{2+} to V^{5+}.[21,22] Generally, insertions of exotic cation occur at the six-fold oxygen coordinated site inside the a-b plane of α-V_2O_5. Unfortunately, because of its compact interlayer space of a-b plane (4.379 Å), in which single V–O layers composed of VO_5 square pyramids are tightly arranged,[23,24] the insertion and diffusion of K^+ in α-V_2O_5 have proved to be very difficult. Unlocking the compact crystal structures to create suitable accommodation sites and diffusion paths for K^+ in α-V_2O_5 remains challenging. Theoretically, lowering the oxidation state of vanadium in α-V_2O_5 could induce the transformation of the V–O square pyramids to octahedra, followed by the subsequent rearrangement of the crystal structure into a double-layered structure with a larger interlayer space. As a result, the expanded α-V_2O_5 would allow rapid K-ion diffusion. However, because of the various oxidation states of vanadium, uncontrollable changes in the valence of vanadium always result in an impure product. Nevertheless, even with the ideally reconstructed crystal structure of α-V_2O_5, obtaining maximum utilization of the K-ion storage sites and diffusion channels in real materials is also difficult, especially for the insertion and diffusion of large K ions. Theoretically, because of the weak van der Waals force between each of two V–O layers, the crystal growth along c axis could be suppressed, leading to the crystal expansion within the a-b plane, wherein K-ion storage sites and diffusion channels are located. In consequence, controlling the crystal growth of V–O structure within the a-b plane is the key to efficiently utilizing the K-ion storage sites and diffusion channels. Considering that 1D structured nanomaterials facilitate full use of cation storage sites thanks to their large specific surface area, it is reasonable to believe that 1D structured nanomaterials could significantly improve the K-ion storage capacity. However, in reality, inappropriate growth orientation does not actually shorten the diffusion distance for inserted cation in real materials, such as the diffusions along the growth orientation of 1D structured nanomaterial. Therefore, to achieve the efficient storage and rapid diffusion of K ions in α-V_2O_5, we adopted a two-pronged strategy that combines reconstruction of the crystal structure and design of the morphology with oriented growth.

Herein, as a proof-of-concept experiment, to lower the insertion energetics and diffusion barriers of K^+ via reconstructing the V–O polyhedra of α-V_2O_5, we synthesized single-crystalline bilayered δ-$K_{0.51}V_2O_5$ nanobelts (KVOs) with a large interlayered structure (9.5 Å) and optimized growth orientation ([010] orientation) by using a scalable, facile, and low-cost chemical preintercalation method. When applied in KIBs, the as-prepared KVO delivers a reversible capacity of 131 mAh g^{-1} at an average storage voltage of 3.2 V and superior rate capability even at 10 A g^{-1}. Combined with *ex situ* testing methods, we demonstrate that KVO transforms reversibly into a new phase upon K-ion deintercalation and intercalation. Density functional theory (DFT) calculations further revealed that the large interlayered structure and unique 1D morphology along the [010] orientation are responsible for the ultrahigh rate performance. In addition, we also assembled full KVO-graphite KIBs that exhibit high energy (238 Wh kg^{-1}) and power (5,480 W kg^{-1}) densities (based on the mass of cathodes). These promising electrochemical results and insight into the K-storage mechanism brings low-cost room-temperature KIBs a step closer to realization as a sustainable large-scale energy storage system.

RESULTS AND DISCUSSION

Commercial α-V_2O_5 powder has an orthorhombic structure (space group *Pmmn*) with irregular particle morphology (Figure S1). Simple solution treatment by the

[1]Key Laboratory of Automobile Materials, Ministry of Education, Department of Materials Science and Engineering, Jilin University, Changchun 130022, China

[2]State Key Laboratory of Rare Earth Resource Utilization, Changchun Institute of Applied Chemistry, Chinese Academy of Sciences, Changchun 130022, China

[3]Beijing National Laboratory for Condensed Matter Physics, Institute of Physics, Chinese Academy of Sciences, Beijing 100190, China

[4]These authors contributed equally

[5]Lead Contact

*Correspondence: junminyan@jlu.edu.cn
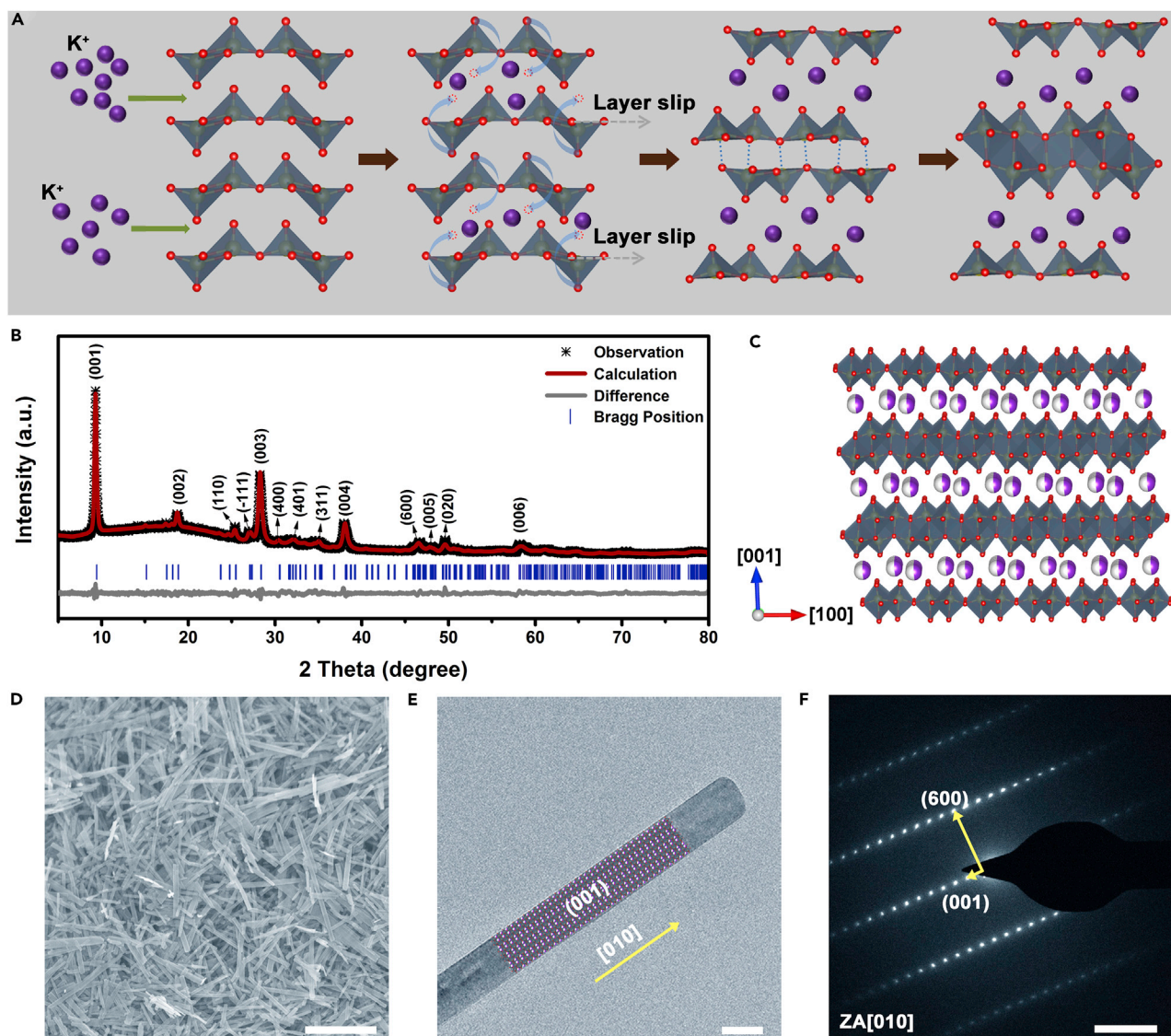
Figure 1. Structure and Morphology of KVO

(A) Schematic diagrams of the structural evolution from α-V_2O_5 to KVO.

(B and C) XRD pattern (B) and schematic representation of the crystal structure (C) of KVO.

(D and E) SEM (D; scale bar, 2 μm) and TEM (E; scale bar, 50 nm) images of KVO.

(F) SAED pattern of a single KVO nanobelt (scale bar, 5 1/nm).

controllable reduction of commercial α-V_2O_5 in K^+-containing solution preferentially produces KVO. Figure 1A clearly shows the mechanism of structural evolution from α-V_2O_5 to KVO.[25,26] First, the insertion and diffusion of K ions into the layers leads to layer slippage. Notably, the distortion at the edge of the lattice makes the insertion process more likely to occur at every two layers. Subsequently, the VO_5 square pyramid would rotate backward following the classic motion of VO_5. Then, driven by the lower thermodynamically energy, the vanadium atoms would rearrange in the lattice and re-bond with the oxygen atoms to form stable VO_6 octahedra. Finally, after this structural evolution process, the KVO layered structure is formed. Rietveld-refined X-ray diffraction (XRD) was used to identify the crystal structure of the as-prepared KVO (Figure 1B). All diffraction peaks in the XRD

patterns can be indexed to the monoclinic phase with space group *C2/m*, indicating phase-pure KVO with no impurities (detailed structural parameters are shown in Table S1 and Figure S2). The X-ray photoelectron spectroscopy (XPS) spectra in Figure S3 further confirm the high purity of the obtained KVO. The corresponding refined structural models are also shown in Figures 1C and S4, where two single sheets of VO_6 polyhedra alternately stack together by edge sharing, yielding a double-layered structure, and the alkali metal atoms are sandwiched in the weakly bound V–O areas. Furthermore, from inductively coupled plasma and thermogravimetric analysis (Figure S5), the composition of the samples is defined as $K_{0.51}V_2O_5$.

The morphologies of KVO were explored by scanning electron microscopy (SEM) and transmission electron microscopy (TEM). As presented in Figures 1D, 1E, and S6, the as-prepared KVO shows a highly regular nanobelt morphology approximately 26–148 nm in width and micrometers in length and grown along the [010] orientation.[25] Each belt is composed of a single-crystalline domain, as shown by selected-area electron diffraction (SAED, Figure 1F), and the set of diffraction spots can be indexed to the (600) and (001) planes along the [010] zone axis. In fact, single-crystal materials possess no significant grain boundaries and few defects, which in principle can facilitate ionic diffusion.[27] Importantly, the (001) facet of the nanobelts is dominant (Figures 1E and 1F) and possesses a large layer distance of 9.5 Å. Theoretically, this kind of large layered structure could provide open and stable channels for facile ion insertion and extraction.

Inspired by the structural and purity advantages, we investigated the electrochemical performance of the KVO toward K by using coin cells with metallic K as the counter electrode. The galvanostatic charge-discharge technique was used to evaluate the electrochemical performance of the KVO. As shown in Figure 2A, the as-prepared bilayered KVO delivered an initial charge capacity of 68.9 mAh g^{-1}. Subsequently, the discharge capacity reached a high level of 131 mAh g^{-1}, corresponding to the insertion of approximately 1 K ion per formula. In the following cycles (Figure S7A), the capacity was almost unchanged, demonstrating excellent electrochemical reversibility. In contrast, the K-ion storage performance of the α-V_2O_5 electrodes (Figure S7B) was very poor, showing a reversible discharge capacity of only 14 mA hr g^{-1}. Apparently, the voltage-capacity profile of the KVO electrodes displayed three distinct plateaus, and the precise potentials were further analyzed with the differential galvanostatic (dQ/dV) curve (Figure 2B). During the discharge process, the KVO electrodes revealed three main peaks at approximately 3.94 (R_1), 3.16 (R_2), and 2.48 V (R_3). During the following charge process, three main peaks at 4.17, 3.21, and 2.91 V were observed, which were assigned to O_1, O_2, and O_3, respectively, corresponding to the R_1, R_2, and R_3 reduction reactions, respectively.

To investigate the reversible structural evolution of KVO upon K^+ insertion and extraction, we performed *ex situ* XRD measurements on the electrodes at different charge-discharge states (Figure 2C), corresponding to points 1–15 in Figure 2A. During the first charge process (from 1 to 3), the peak assigned to (003) exhibited a minor shift to high angle (Figure S8), indicating a decrease in the lattice parameter caused by K^+ extraction. Subsequently, the reverse behavior was observed during potassiation (from 3 to 5). In stage I (from 1 to 5), all patterns remained almost unchanged, implying a single-phase reaction in this region (Figure S8).[28,29] The result was further confirmed by the XRD Rietveld refinement of the fully charged KVO (Figures S9 and S10; Table S2). In the following discharge process
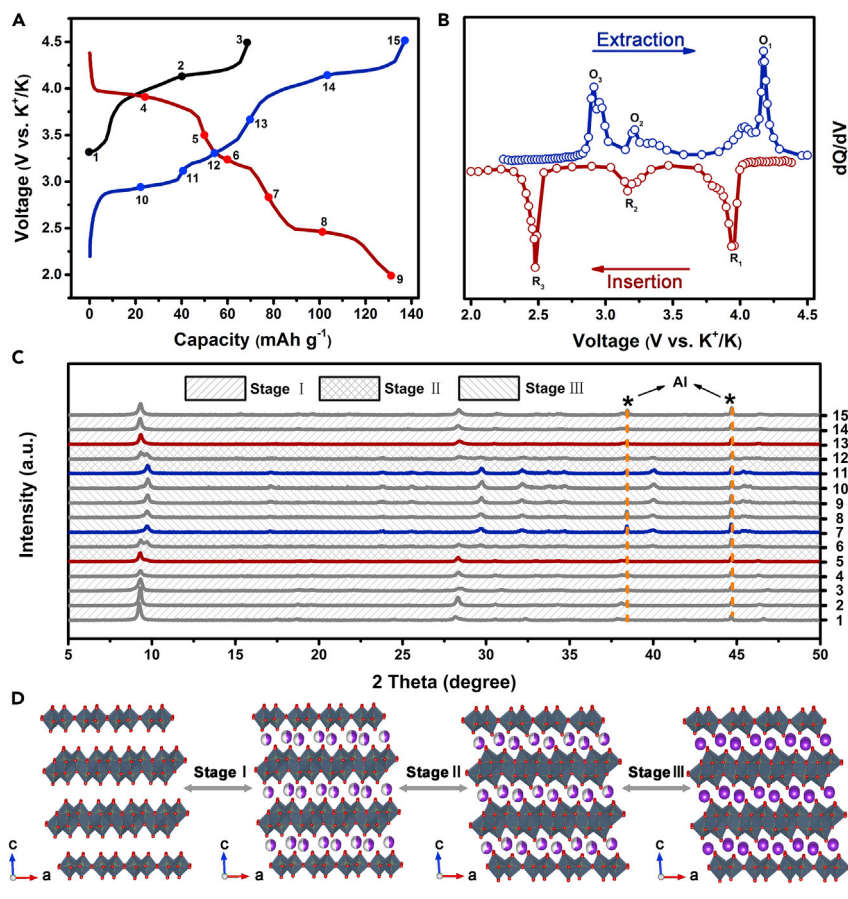
Figure 2. Structural Evolution of Electrochemical Potassiation

(A and B) Galvanostatic charge-discharge curves (A) and the corresponding dQ/dV curves (B) of KVO at a current density of 30 mA g^{-1}.

(C) *Ex situ* XRD patterns of the KVO electrodes at the different states in (A).

(D) Structural evolution of KVO upon K$^+$ insertion and extraction.

(from 5 to 7), the peaks corresponding to δ-K$_x$V$_2$O$_5$ became less intense and gradually disappeared, and some new peaks appeared (Figure S11). In stage II (from 5 to 7), a new phase (denoted as n-K$_x$V$_2$O$_5$) was generated and the old phase (δ-K$_x$V$_2$O$_5$) disappeared, indicating the formation of a biphasic domain.[29] Finally, at the end of potassiation (from 7 to 9), all patterns remained nearly unchanged, indicating that K$^+$ insertion and extraction occur in stage III via a single-phase reaction (Figure S12). Additionally, on the basis of XRD Rietveld refinement of the fully discharged KVO, the n-K$_x$V$_2$O$_5$ can be indexed to the monoclinic phase with space group C2/m (Figures S13 and S14; Table S3). Although the length of the V–O bond changed significantly, the n-K$_x$V$_2$O$_5$ still maintained a bilayered structure, meaning a stable structure for accommodation of the K ion. More importantly, the reverse behavior was observed in the second charge process, where the XRD pattern returned to the pristine state at the end of charging, demonstrating the structural reversibility of KVO. Meanwhile, we employ TEM to identify the morphology change of KVO upon K$^+$ insertion and extraction. As shown in Figure S15, the nanobelts were found in both fully charged (Figure S15A) and discharged (Figure S15C) KVO electrodes. In the fully charged KVO electrodes, the lattice fringes of 9.4 Å were observed (Figure S15B), corresponding to the (001) planes of δ-V$_2$O$_5$. In the fully discharged KVO

electrodes, the lattice fringes of 9.0 Å were found (Figure S15D), which originated from (001) planes of n-KV$_2$O$_5$. In conclusion, the KVO underwent a single-phase reaction (δ-V$_2$O$_5$ to δ-K$_x$V$_2$O$_5$), a phase-transition reaction (δ-K$_x$V$_2$O$_5$ to n-K$_x$V$_2$O$_5$), and a subsequent single-phase reaction (n-K$_x$V$_2$O$_5$ to n-KV$_2$O$_5$) upon K$^+$ insertion and extraction, as shown in Figure 2D.

To further study the phase change of KVO upon K$^+$ insertion and extraction, we employed XPS on KVO at different charge-discharge states (Figures S16 and S17). As shown in Figure S17, the high-resolution V2p 3/2 spectrum of all examples was deconvoluted into two regions: V^{5+} (at approximately 517.7 eV) and V^{4+} (at approximately 516.3 eV).[25] During charging, the peak assigned to V^{5+} increased in intensity, whereas the peak attributed to V^{4+} decreased in intensity. During discharging, the reverse behavior was observed, indicating that the reversible vanadium interchange from V^{5+} to V^{4+} dominated the K-ion insertion and extraction process.

From the *ex situ* XRD and XPS analyses, we demonstrated that KVO can provide a stable crystal framework during K-ion insertion and extraction. As shown in Figure 3A, the KVO electrodes delivered remarkably high rate capability. As the current density increased from 0.05 to 0.2, 0.4, 1, 2, and 6 A g^{-1}, the KVO electrode delivered good capacity retention, varying from 125 to 117, 107, 97, 89, and 76 mA hr g^{-1}, respectively. Remarkably, even at a high rate of 10 A g^{-1}, the reversible capacity still reached 64 mA hr g^{-1}, corresponding to 51.2% capacity retention. To evaluate possible practical applications of the KVO cathode, we calculated its power (rate) and energy density on the basis of its working potential and capacity at various rates and the mass of the cathode material; this value is represented in a Ragone plot together with those of other advanced KIBs cathodes (Figure 3B; Table S4). The KVO cathode exhibited a high gravimetric energy of 397 W hr kg^{-1} at a low specific power of 0.16 kW kg^{-1} and was able to maintain 50% of the energy (198 W hr kg^{-1}) when the power was increased 2 orders of magnitude (30.82 kW kg^{-1}). Such performance is significantly better than that of current state-of-the-art cathodes in KIBs, such as KVPO$_4$F,[13] K$_3$V$_2$(PO$_4$)$_3$/C,[14] KFe^{II}[Fe^{III}(CN)$_6$],[15] K$_{1.6}$Mn[Fe(CN)$_6$]$_{0.96}$·0.27H$_2$O,[16] K$_{0.7}$Fe$_{0.5}$Mn$_{0.5}$O$_2$,[17] K$_{0.6}$CoO$_2$,[18] K$_{0.5}$MnO$_2$,[19] and K$_{0.5}$V$_2$O$_5$,[20] indicating that our KVO is a very promising candidate for building superior electrochemical energy storage devices with both high power density and high energy density. Inspired by the excellent rate capability of KVO, we then tested the cycling stability under high current densities. As shown in Figures 3C and S18, the KVO electrodes exhibited stable capacities of 77.8, 51.4, and 45.6 mAhg^{-1} at current densities of 0.1, 2, and 4 A g^{-1}, respectively, even after 100 cycles. These correspond to 61.3%, 60.5%, and 60.7% of the initial reversible capacity, respectively.

To gain further insight into the underlying mechanism of the aforementioned outstanding electrochemical performance, we investigated the K-insertion energetics, electronic structures, and K-diffusion barriers for δ-V$_2$O$_5$ and α-V$_2$O$_5$ by using DFT. Note that we constructed the calculated structure of δ-V$_2$O$_5$ by removing the K of δ-K$_{0.51}$V$_2$O$_5$ and then performing structure optimization (Figure S19). From the results of the theoretical calculations (Figures S20–S22; Table S5), we found that bilayered δ-V$_2$O$_5$ is a more attractive cathode material for KIBs than α-V$_2$O$_5$ because of the more suitable insertion site for K ions (Figure S20; Table S5), higher electronic conductivity (Figure S21), and more favorable electron structure (Figure S22).

To examine the potassiation dynamics, we investigated the K-diffusion barriers of various trajectories for α-V$_2$O$_5$ and δ-V$_2$O$_5$ by the climbing image nudged elastic band (CI-NEB) method.[30] As shown in Figure S23, α-V$_2$O$_5$ exhibited two typical
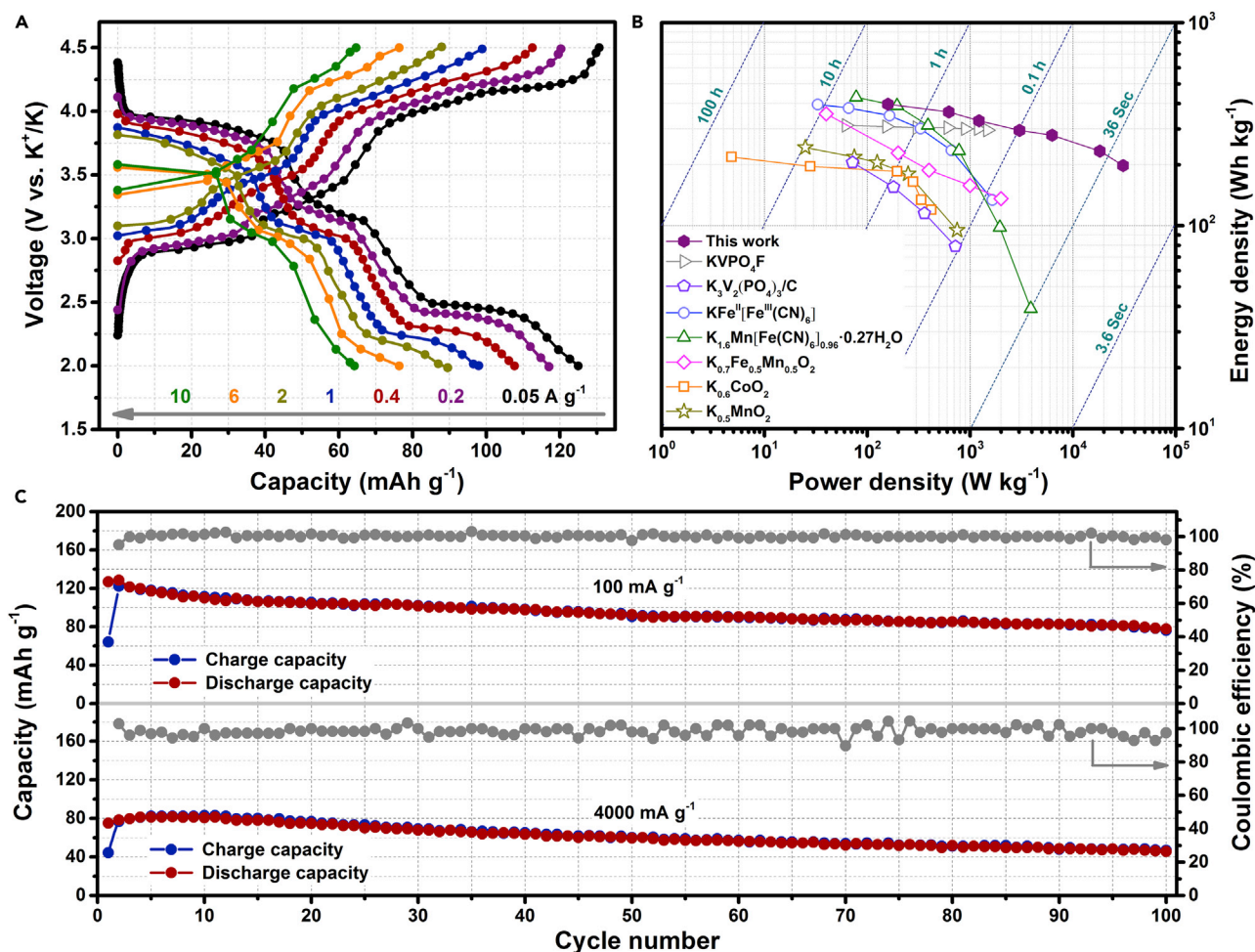
Figure 3. K Storage Performance of KVO

(A) Charge-discharge curves of the KVO electrodes at different current densities.

(B) Ragone plots of our KVO cathode other advanced KIB cathodes, including $KVPO_4F$, $K_3V_2(PO_4)_3/C$, $KFe^{II}[Fe^{III}(CN)_6]$, $K_{1.6}Mn[Fe(CN)_6]_{0.96}\cdot0.27H_2O$, $K_{0.7}Fe_{0.5}Mn_{0.5}O_2$, $K_{0.6}CoO_2$, $K_{0.5}MnO_2$, and $K_{0.5}V_2O_5$.

(C) Cycle performance of the KVO electrodes at different current densities.

K-diffusion paths along the x and z directions with diffusion barriers of 1.78 and 5.40 eV (Figures S24–S26), respectively. In contrast, δ-V_2O_5 possessed three possible paths, two of which, named path 1 and path 2, were in the interlayer of the (001) lattice plane (Figures 4A and 4C) and one of which (path 3) was along the [001] orientation (Figure S27). For K-ion diffusion through path 1 (Figures 4A and 4B), the diffusion direction was along the [010] orientation (1→2→3→4), and the results showed that K atoms diffused from the different points with the same energy barrier of 0.89 eV (Figures 4B, S28, and S29). For path 2 (Figures 4C and 4D), K atoms first diffused from site 1 to site 2 with an energy barrier of 0.85 eV (Figures S28 and S30). As K atoms diffused further from the site 2 to site 3, the energy barrier decreased to 0.08 eV (Figures S28 and S31). When K ions diffused through path 3, as shown in Figures S27, S28, and S32, the large energy barrier (6.58 eV) to pass from site 1 to site 2 prohibited K diffusion along the [001] orientation at room temperature. Notably, both α-V_2O_5 and δ-V_2O_5 possessed a large energy barrier along the [001] orientation, which was probably due to the obvious increase in the interlayer spacing and expansion of the diffusion tunnel during diffusion (Figures S26 and S32). Overall, δ-V_2O_5
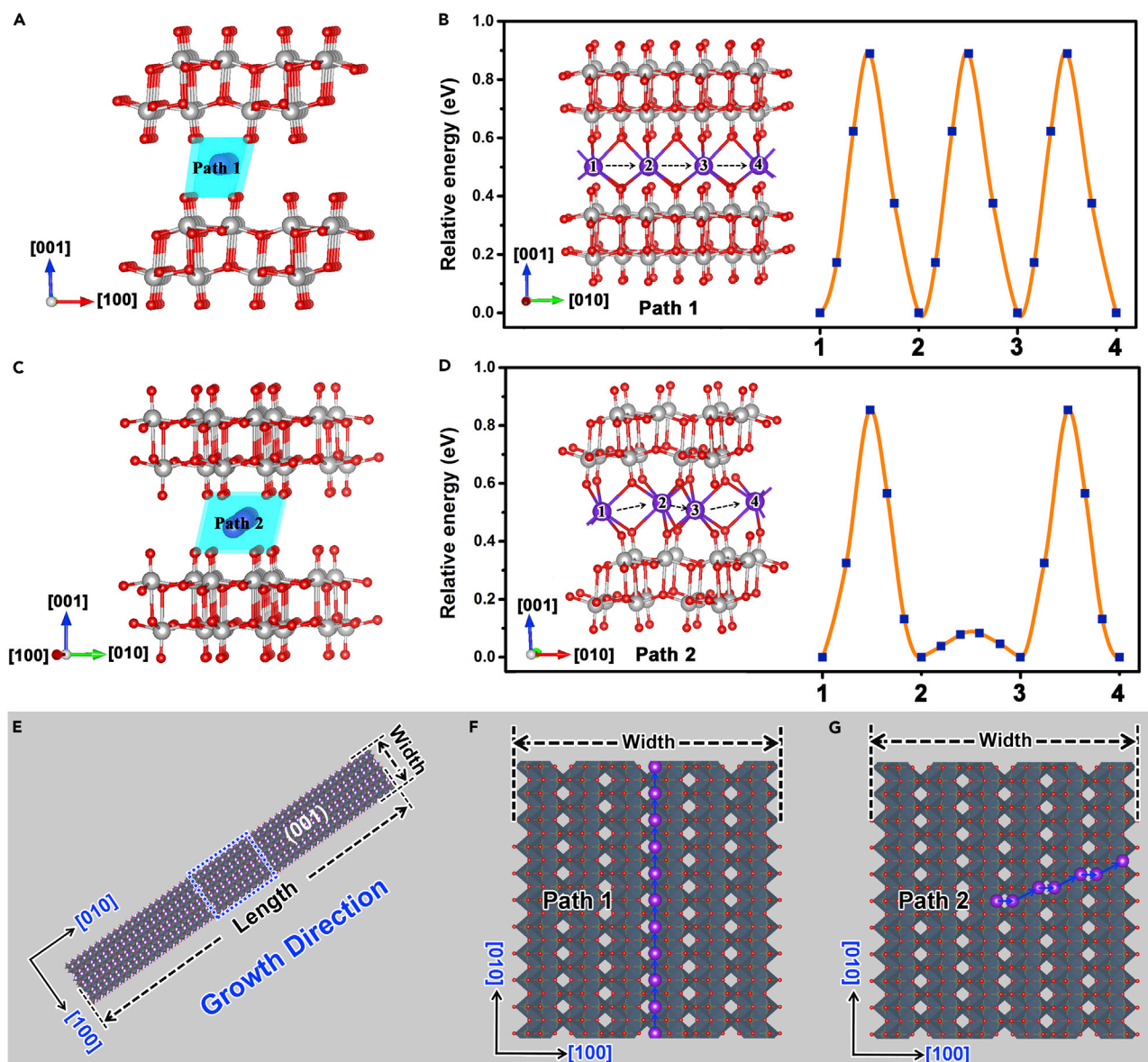
Figure 4. Diffusion Pathways for K Ions in KVO

(A–D) K-ion diffusion pathways (A and C) and the corresponding migration activation energy (B and D) through the interlayer of the (001) lattice plane of δ-V_2O_5.

(E) Structure of the as-prepared bilayered δ-$K_{0.51}V_2O_5$ nanobelts.

(F and G) Schematic diagram of the diffusion of K ions through path 1 (F) and path 2 (G) in the selected area of (E).

possessed a larger number of K-ion diffusion tunnels, and these tunnels had lower diffusion barriers than those of α-V_2O_5. The rich and fast K-ion diffusion channels in δ-V_2O_5 led to superior rate performance.

Notably, δ-$K_{0.51}V_2O_5$ nanobelts grew along the [010] direction, as shown in Figure 4E. Assuming that each nanobelt has an average length of l and an average width of d, when K ions diffuse along the [001] orientation in path 1, the average diffusion distance is 0.5l. In contrast, when K ions diffuse along path 2, the average diffusion distance is 0.53d (for a detailed calculation process, see Figure S33). As mentioned above, the δ-$K_{0.51}V_2O_5$ nanobelts had an average width of 74 nm (inset in Figure S6A) and a length
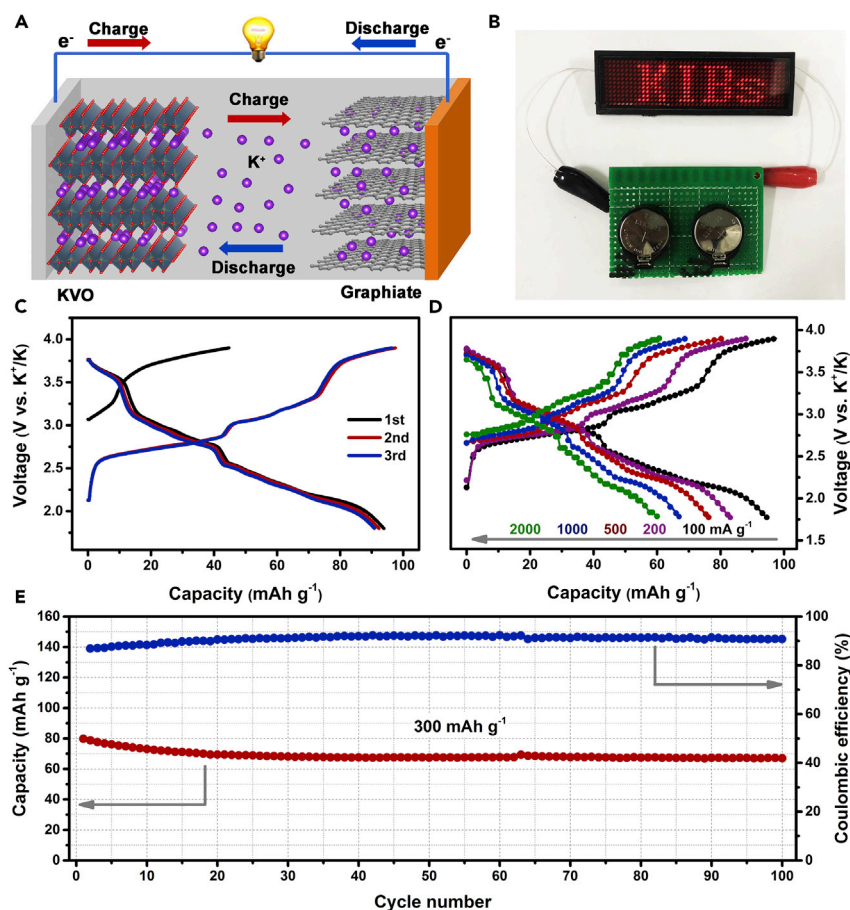
Figure 5. Demonstration of a K-Ion Full Battery

(A) Schematic illustration of the K-ion full cell.

(B) Lit LED screen driven by K-ion full batteries.

(C) Galvanostatic charge-discharge curves of the K-ion full batteries at a current density of 100 mA g^{-1}.

(D) Galvanostatic charge-discharge curves of the K-ion full batteries at different current densities.

(E) Cycle performance of the K-ion full batteries at a current density of 300 mA g^{-1}.

in micrometers, indicating that the diffusion distance along path 1 would be approximately 100 times (or more) that of path 2. The diffusion time (τ), diffusion distance (L), and diffusion coefficient (D) can be described by the following equation:[31,32]

$$\tau = L^2/D.$$

Because the diffusion coefficient (D) of path 2 is larger than that of path 1 as a result of the smaller diffusion barriers of path 2, the diffusion time of path 1 is 10,000 times longer than that of path 2. These results indicate that diffusion along path 2 is mainly responsible for the ultrahigh rate performance of KVO.

In real applications, a metallic K battery would be highly dangerous and unrealistic because of the high activity of K metal. Therefore, we demonstrated a rocking-chair K-ion full battery with KVO as the cathode and potassiated graphite as the anode (for detailed information, see Figure S34). During the charge process, K ions were extracted from KVO and inserted into graphite, and the reverse behavior occured upon discharging (Figure 5A). The lit LED screen powered by the K-ion full cell indicates that this energy system is feasible (Figure 5B). As shown in Figure 5C, the full

battery delivered a reversible capacity of 94 mAh g^{-1} (based on the mass of the cathode) with a mean operating voltage of 2.53 V, corresponding to a high energy density of approximately 238 Wh kg^{-1} (based on the mass of cathodes). In addition, this full cell also exhibited superior rate capability (Figure 5D) and cycle performance (Figures 5E and S35). As shown in Figure 5D, a reversible capacity of 60 mA hr g^{-1} could be reached even at a high current rate of 2 A g^{-1}, corresponding to 64% capacity retention. Meanwhile, the good capacity retention of 84% after 100 cycles manifests the considerable long-term cycling stability of our full cell (Figure 5E). More importantly, in the Ragone plot shown in Figure S36, the full cell has both higher energy (238 Wh kg^{-1}) and power (5480 W kg^{-1}) densities (based on the mass of cathodes) than most reported full KIBs (Table S6). Such superior electrochemical performance suggests promising applications of KVO in full KIBs for large-scale energy storage systems.

In summary, as a proof-of-concept experiment, to alleviate the high insertion energetics and diffusion barriers of K ions through the reconstruction of V–O polyhedra of α-V$_2$O$_5$, we synthesized single-crystalline bilayered KVO with an optimized growth orientation along the [010] direction to form a stable bilayered structure to endure reversible K-ion insertion and extraction via a facile chemical preintercalation synthetic approach by using low-cost α-V$_2$O$_5$ as the raw material. The as-prepared KVO has a large layered structure (9.5 Å) and 1D nanobelt morphology, which could theoretically facilitate K-ion insertion, extraction, and diffusion. When used as the cathode material for KIBs, between 2 and 4.5 V, KVO exhibits superior K-storage performance, including high average voltage (3.2 V), high capacity (131 mAh g^{-1}), and superior rate capability even at 10 A g^{-1}. The combined analysis of *ex situ* XRD and XPS reveals that the δ phase of K$_{0.51}$V$_2$O$_5$ transforms reversibly into a new phase upon K-ion deintercalation and intercalation. Additionally, DFT calculations indicate that the excellent K-ion storage performance of KVO could be attributed to its large interlayered structure and unique 1D morphology along the [010] orientation, which lead to low diffusion barriers and short diffusion distances, allowing rapid K-ion diffusion inside the layer. More importantly, we also proposed and demonstrated a rocking-chair full cell with KVO as the cathode material and graphite as the anode material, which exhibits a high energy density (238 Wh kg^{-1}) and a high power density (5,480 W kg^{-1}) (based on the mass of cathodes). We believe that the promising electrochemical results obtained herein, as well as the insight into the K-storage mechanisms, brings low-cost room-temperature KIBs a step closer to becoming sustainable large-scale energy storage systems.

EXPERIMENTAL PROCEDURES

Full experimental procedures are provided in the Supplemental Information.

SUPPLEMENTAL INFORMATION

Supplemental Information includes Supplemental Experimental Procedures, 36 figures, and 6 tables and can be found with this article online at https://doi.org/10.1016/j.chempr.2018.10.004.

AUTHOR CONTRIBUTIONS

Y.-H.Z. and J.-M.Y. designed this work; Y.-H.Z. conducted the electrochemical experiment; Q.Z. performed the first-principle calculations; X.Y., E.-Y.Z., and X.-Q.Y. refined the XRD results; Y.-H.Z. and J.-M.Y. wrote the paper; and all authors participated in the analysis of the experimental data, discussion of the results, and preparation of the paper.

DECLARATION OF INTERESTS

The authors declare no competing interests.

REFERENCES AND NOTES

1. Tarascon, J.M., and Armand, M. (2001). Building better batteries. Nature *414*, 359–367.

2. Scrosati, B., and Garche, J. (2010). Lithium batteries: status, prospects and future. J. Power Sources *195*, 2419–2430.

3. Zhu, Y.H., Yuan, S., Bao, D., Yin, Y.B., Zhong, H.X., Zhang, X.B., Yan, J.M., and Jiang, Q. (2017). Decorating waste cloth via industrial wastewater for tube-type flexible and wearable sodium-ion batteries. Adv. Mater. *29*, https://doi.org/10.1002/adma.201603719.

4. Xiao, N., McCulloch, W.D., and Wu, Y. (2017). Reversible dendrite-free potassium plating and stripping electrochemistry for potassium secondary batteries. J. Am. Chem. Soc. *139*, 9475–9478.

5. Aurbach, D., Lu, Z., Schechter, A., Gofer, Y., Gizbar, H., Turgeman, R., Cohen, Y., Moshkovich, M., and Levi, E. (2000). Prototype systems for rechargeable magnesium batteries. Nature *407*, 724–727.

6. Lin, M.C., Gong, M., Lu, B., Wu, Y., Wang, D.Y., Guan, M., Angell, M., Chen, C., Yang, J., Hwang, B.J., and Dai, H. (2015). An ultrafast rechargeable aluminium-ion battery. Nature *520*, 324–328.

7. Komaba, S., Hasegawa, T., Dahbi, M., and Kubota, K. (2015). Potassium intercalation into graphite to realize high-voltage/high-power potassium-ion batteries and potassium-ion capacitors. Electrochem. Commun. *60*, 172–175.

8. Wu, X., Leonard, D.P., and Ji, X. (2017). Emerging non-aqueous potassium-ion batteries: challenges and opportunities. Chem. Mater. *29*, 5031–5042.

9. Zhang, W., Pang, W.K., Sencadas, V., and Guo, Z. (2018). Understanding high-energy-density Sn4P3 anodes for potassium-ion batteries. Joule *2*, 1534–1547.

10. Zhang, W., Mao, J., Li, S., Chen, Z., and Guo, Z. (2017). Phosphorus-based alloy materials for advanced potassium-ion battery anode. J. Am. Chem. Soc. *139*, 3316–3319.

11. Zhu, Y.H., Yin, Y.B., Yang, X., Sun, T., Wang, S., Jiang, Y.S., Yan, J.M., and Zhang, X.B. (2017). Transformation of rusty stainless-steel meshes into stable, low-cost, and binder-free cathodes for high-performance potassium-ion batteries. Angew. Chem. Int. Ed. *56*, 7881–7885.

12. Zhang, C., Xu, Y., Zhou, M., Liang, L., Dong, H., Wu, M., Yang, Y., and Lei, Y. (2017). Potassium Prussian blue nanoparticles: a low-cost cathode material for potassium-ion batteries. Adv. Funct. Mater. *27*, 1604307.

13. Chihara, K., Katogi, A., Kubota, K., and Komaba, S. (2017). KVPO4F and KVOPO4 toward 4 volt-class potassium-ion batteries. Chem. Commun. (Camb). *53*, 5208–5211.

14. Han, J., Li, G.N., Liu, F., Wang, M., Zhang, Y., Hu, L., Dai, C., and Xu, M. (2017). Investigation of K3V2(PO4)3/C nanocomposites as high-potential cathode materials for potassium-ion batteries. Chem. Commun. (Camb). *53*, 1805–1808.

15. Chong, S., Chen, Y., Zheng, Y., Tan, Q., Shu, C., Liu, Y., and Guo, Z. (2017). Potassium ferrous ferricyanide nanoparticles as a high capacity and ultralong life cathode material for nonaqueous potassium-ion batteries. J. Mater. Chem. A *5*, 22465–22471.

16. Jiang, X., Zhang, T., Yang, L., Li, G., and Lee, J.Y. (2017). A Fe/Mn based Prussian blue analogue as a K-rich cathode material for potassium-ion batteries. ChemElectroChem *4*, 2237–2242.

17. Wang, X., Xu, X., Niu, C., Meng, J., Huang, M., Liu, X., Liu, Z., and Mai, L. (2017). Earth abundant Fe/Mn-based layered oxide interconnected nanowires for advanced K-ion full batteries. Nano Lett. *17*, 544–550.

18. Kim, H., Kim, J.C., Bo, S.H., Shi, T., Kwon, D.H., and Ceder, G. (2017). K-ion batteries based on a P2-type K0.6CoO2 cathode. Adv. Energy Mater. *7*, 1700098.

19. Kim, H., Seo, D.H., Kim, J.C., Bo, S.H., Liu, L., Shi, T., and Ceder, G. (2017). Investigation of potassium storage in layered P3-Type K0.5MnO2 cathode. Adv. Mater. *29*, 1702480.

20. Deng, L., Niu, X., Ma, G., Yang, Z., Zeng, L., Zhu, Y., and Guo, L. (2018). Layered potassium vanadate K0.5V2O5 as a cathode material for nonaqueous potassium ion batteries. Adv. Funct. Mater. https://doi.org/10.1002/adfm.201800670.

21. Liu, J., Xia, H., Xue, D., and Lu, L. (2009). Double-shelled nanocapsules of V2O5-based composites as high-performance anode and cathode materials for Li ion batteries. J. Am. Chem. Soc. *131*, 12086–12087.

22. Raju, V., Rains, J., Gates, C., Luo, W., Wang, X., Stickle, W.F., Stucky, G.D., and Ji, X. (2014). Superior cathode of sodium-ion batteries: orthorhombic V2O5 nanoparticles generated in nanoporous carbon by ambient hydrolysis deposition. Nano Lett. *14*, 4119–4124.

23. Koch, D., Kulish, V.V., and Manzhos, S. (2017). A first-principles study of potassium insertion in crystalline vanadium oxide phases as possible potassium-ion battery cathode materials. MRS Commun. *7*, 819–825.

24. Parija, A., Prendergast, D., and Banerjee, S. (2017). Evaluation of multivalent cation insertion in single-and double-layered polymorphs of V2O5. ACS Appl. Mater. Interfaces *9*, 23756–23765.

25. Xu, K., Hu, S., Wu, C., Lin, C., Lu, X., Peng, L., Yang, J., and Xie, Y. (2012). Highly entangled K0.5V2O5 superlong nanobelt membranes for flexible nonvolatile memory devices. J. Mater. Chem. *22*, 18214–18220.

26. Patridge, C.J., Wu, T.L., Jaye, C., Ravel, B., Takeuchi, E.S., Fischer, D.A., Sambandamurthy, G., and Banerjee, S. (2010). Synthesis, spectroscopic characterization, and observation of massive metal insulator transitions in nanowires of a nonstoichiometric vanadium oxide bronze. Nano Lett. *10*, 2448–2453.

27. Dai, K., Mao, J., Li, Z., Zhai, Y., Wang, Z., Song, X., Battagli, V., and Liu, G. (2014). Microsized single-crystal spinel LAMO for high-power lithium ion batteries synthesized via polyvinylpyrrolidone combustion method. J. Power Sources *248*, 22–27.

28. Zhu, Y.H., Yang, X., Bao, D., Bie, X.F., Sun, T., Wang, S., Jiang, Y.S., Zhang, X.B., Yan, J.M., and Jiang, Q. (2018). High-energy-density flexible potassium-ion battery based on patterned electrodes. Joule *2*, 736–746.

29. Berthelot, R., Carlier, D., and Delmas, C. (2011). Electrochemical investigation of the P2-Na_xCoO_2 phase diagram. Nat. Mater. *10*, 74–80.

30. Henkelman, G., Uberuaga, B.P., and Jónsson, H. (2000). A climbing image nudged elastic band method for finding saddle points and minimum energy paths. J. Chem. Phys. *113*, 9901–9904.

31. Gleiter, H. (1992). Diffusion in nanostructured metals. Phys. Status Solidi B *172*, 41–51.

32. Levi, M.D., and Aurbach, D. (1997). Diffusion coefficients of lithium ions during intercalation into graphite derived from the simultaneous measurements and modeling of electrochemical impedance and potentiostatic intermittent titration characteristics of thin graphite electrodes. J. Phys. Chem. B *101*, 4641–4647.